Soft Matter

Cite this: *Soft Matter*, 2011, **7**, 11392

www.rsc.org/softmatter

PAPER

Penetration of lipid bilayers by nanoparticles with environmentally-responsive surfaces: simulations and theory

Reid C. Van Lehn and Alfredo Alexander-Katz*

Received 22nd July 2011, Accepted 5th October 2011
DOI: 10.1039/c1sm06405c

Understanding the interactions between nanoparticles (NPs) and lipid bilayers is critical for the design of drug delivery carriers, biosensors, and biocompatible materials. In particular, it is desirable to understand how to effectively translocate synthetic molecules through the cellular membrane, which acts as a selective barrier to regulate transport into the cell. In this work, we use simulations and theory to explore the role that surface reconstruction may play in non-specific interactions between NPs and lipid bilayers. We show that NPs with a mixed hydrophobic/hydrophilic surface functionalization capable of rearranging their surfaces to maximize hydrophobic matching with the bilayer core are able to spontaneously establish a thermodynamically-favored position at the bilayer midplane. Furthermore, this penetration behavior is most favorable thermodynamically when the surface of the NP is near an order-disorder transition. Our analysis provides design criteria for future synthetic NPs, with the goal of designing particles that can maintain a stable transmembrane orientation.

1 Introduction

The cellular membrane plays an essential role in controlling the transport of external molecules into the cell interior. In biological systems, the membrane acts as a selective barrier that only permits the passage of certain molecules, regulated by a variety of transmembrane protein channels and receptors that target desired ligands. Non-specific, non-disruptive penetration of the membrane without protein mediation is typically achievable only by small molecules.[1–3] Larger objects that bypass the membrane *via* interactions with lipids, like cell-penetrating peptides, generally induce significant disruption of the lipid bilayer structure.[4,5] There is considerable interest in discovering methods to translocate synthetic objects into and through the membrane for drug delivery, biosensing, and other applications, but without permanently disrupting the membrane and potentially triggering cell death.[6,7]

Recently,[8] it was shown that nanoparticles (NPs) coated with a structured surface monolayer of hydrophobic and hydrophilic ligands were capable of non-specifically penetrating biological membranes in an energy-independent process, without showing evidence of endocytosis, poration, or cytotoxicity. Penetration thus appeared to occur *via* interaction between NPs and the lipid bilayer itself as the process did not involve interactions with transmembrane receptors and occurred in multiple distinct cell types. Penetration is surprising given the large number of charged ligands present in the monolayer,[9] which make the NPs soluble in aqueous solvent but also present a seemingly large energy barrier for moving charged groups through the hydrophobic bilayer core.[10–12] An explanation for how these NPs move across the bilayer has yet to be found in the literature, but Verma *et al.* suggested that the surface morphology of the NPs may play a critical role.[8]

Similar interactions between NPs and lipid bilayers have been studied extensively in recent years using atomistic and coarse-grained simulations. Many studies have focused on the role of non-specific behavior such as surface charge,[13–18] which is known to disrupt and induce poration in bilayers. Surface morphology has been explored by studying particles with mixed hydrophobic/hydrophilic surfaces, which exhibit dramatically different free energy barriers when pushed through a bilayer as a function of the number of hydrophilic ligands,[19–21] and studying Janus particles, which have been shown to stabilize existing bilayer pores.[22] Shape was examined as a physical parameter by simulating anisotropic particles, which showed preferential penetration over spherical particles,[23] and by modeling carbon nanotubes and their influence on the surrounding bilayer.[24,25] Finally, several studies have focused on simulations of more specific systems, including curved proteins,[26] HIV,[27] ligand-coated NPs,[28]and DNA-grafted nanoparticles.[29] For more examples, the reader is referred to a recent review.[30] The wealth of work in this field underlines the importance of further understanding NP-bilayer interactions, and especially the role of NP surface characteristics.

These studies suggest that highly charged surfaces in general lead to strong bilayer perturbations, while surfaces that are more hydrophobic in nature can achieve the type of non-disruptive penetration observed in ref. 8. The previous simulation studies are also self-similar in that they represent NP surfaces as largely

---

Massachusetts Institute of Technology, Cambridge, MA, USA. E-mail: aalexand@mit.edu

fixed, without the possibility of significant conformational changes. However, simulations of transmembrane proteins have shown that charged amino acid side chains undergo significant rearrangement to avoid contact with the hydrophobic bilayer core, a process called "snorkeling".[12,31] Similarly, recent work on lipid bilayer-wrapped silica NPs has shown that the fluid bilayer surface permits the rearrangement of ligands for enhanced targeting specificity.[32] In both of these examples, the key property of the system is the ability to dynamically adjust to the presence of the bilayer.

In this work, we propose a new motif for designing synthetic NPs that non-specifically target the characteristic amphiphilic nature of lipid bilayer. The key assumption of our work is that the surface of the NP is composed of a mixture of hydrophobic and hydrophilic ligands that are capable of rearranging to maximize favorable interactions with the hydrophobic core. Environmentally-responsive behavior of this sort has been observed in other soft matter systems, including surfaces grafted with polymer brushes[33] or alkanethiol monolayers,[34] and in principle may apply to several other physical systems as well. We especially focus on NPs that have a diameter on the order of 10 nm and are therefore larger than the hydrophobic core of the bilayer, thus approximating the size of NPs described in the literature. By permitting the dynamic restructuring of the NP surface, we show that penetration can be achieved when the surface of the NP is near an order-disorder transition (ODT) such that the barrier for surface rearrangement is low, enabling the formation of a thermodynamically-favorable NP-bilayer complex. We have additionally developed a mean-field theory to confirm this result independent of the simulation methods. Furthermore, we discuss several model systems that may display this type of ODT under experimentally obtainable conditions and hence may serve as model systems for observing environmentally-responsive penetration behavior.

2 Simulation methods

2.1 Modeling NP surface rearrangement

In this model, we consider the behavior of spherical NPs coated with ligands capable of dynamically rearranging on the NP surface in response to the surrounding environment. It is assumed that all ligands are either hydrophobic or hydrophilic such that exposure to the hydrophobic core is energetically favorable for the former and unfavorable for the latter. To put the model in the most general terms possible, the physical mechanism of rearrangement is not explicitly defined (though several example systems that may exhibit this type of responsive behavior are outlined in Sec. 6), and instead the surface is rearranged to minimize an effective surface energy which is a function of the composition of the surface, the positions of ligands, and the surrounding environment of each ligand. Because ligands are able to rearrange on the surface, the surface exhibits phase behavior that is biased by contact with the hydrophobic bilayer core.

A simple Ising model is used to represent the NP surface energy based on the interactions between the ligands. Interactions with the bilayer are included by treating the hydrophobic core as an effective field that adds a term to the energy of each ligand with a sign dependent on whether the ligand is hydrophilic or hydrophobic. The energy of ligand i is then

$$E_i = B_i - \lambda \sum_{j \in n(i)} \sigma_i \sigma_j \tag{1}$$

where B_i is the effective field acting on the ligand due to the hydrophobic core, $n(i)$ is the set of nearest-neighbors for ligand i, λ is a parameter defining the strength of the interaction between near-neighbor ligands, and σ is the "spin" of the ligand, defined as $+1$ if the ligand is hydrophilic, and -1 if the ligand is hydrophobic. B_i is defined as 0 for all ligands that do not interact with the hydrophobic core, positive for hydrophilic ligands exposed to the core, and negative for hydrophobic ligands exposed to the core, essentially making it an interfacial energy term. The total energy of the surface is equal to the sum over all ligands on the surface.

The critical parameter in the Ising model is λ, which determines interactions between neighboring ligands. The value of λ gives rise to surface phase behavior when the NP is not in contact with the bilayer ($B_i = 0$ for all i). If $\lambda < 0$, the surface energy is minimized by mixing hydrophobic/hydrophilic ligands, while if $\lambda > 0$ phase separation is energetically preferred leading to Janus particles. Because the rearrangement process permits many states of the surface that have an identical surface energy but distinct ligand positions, there is also a configurational entropy contribution to the total free energy of the surface that favors the homogeneous state. Due to this entropy term, the ODT between the homogeneous and heterogeneous state occurs for a critical value $\lambda_c > 0$. Fig. 1 shows simulation snapshots of these two initial surface morphologies expected for NPs prior to exposure to the bilayer as determined by Monte Carlo sampling. It should also be emphasized that upon contact with the bilayer, the parameter B_i in eqn (1) will no longer be 0 and as a result the NP will not necessarily maintain one of these two morphologies. However, λ_c is calculated when there is no contact with the bilayer and hence is strictly a function of the NP surface characteristics. The method for calculating λ_c for the ODT observed on the surface is discussed in the next section.

2.2 Coarse-grained model of NP-bilayer system

Coarse-grained simulations were used to model the translocation of a single NP with a dynamically rearranging surface into a lipid

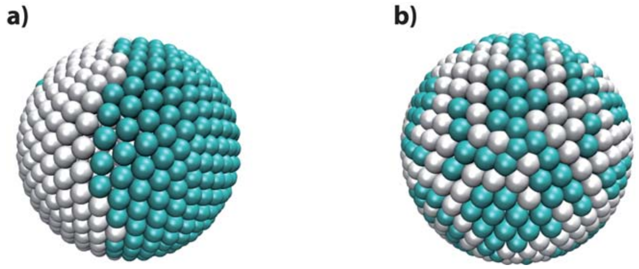

Fig. 1 Simulation snapshots of NPs with their initial surface configurations prior to bilayer interactions. The critical value of λ_c for an ODT on the surface was found by measuring fluctuations in the surface energy, which spikes near the transition. λ_c was measured as 0.32 for a hydrophilic phase fraction ϕ of 0.5, and 0.38 for ϕ of 0.4 or 0.6. **a)** Phase separated state, corresponding to $\lambda > \lambda_c$. **b)** Mixed state, corresponding to $\lambda < \lambda_c$.

bilayer. An implicit solvent bilayer model first developed by Cooke *et al.*[35,36] was chosen because it has been previously used to model interactions with other external objects, including cell penetrating peptides[37] and viruses.[26] Each lipid was modeled as a hydrophilic head bead and two hydrophobic tail beads joined by harmonic springs, with an additional spring potential between the first and third bead to limit bending. The diameter of all beads was set by a repulsive Weeks-Chandler-Anderson potential,

$$U_{rep}(r) = \begin{cases} 4\varepsilon\left[(b/r)^{12} - (b/r)^{6} + 1/4\right] & r \leq r_c \\ 0 & r > r_c \end{cases} \tag{2}$$

This sets r_c as the diameter of the beads, with $r_c = 2^{1/6}b$. To reflect the larger size of lipid tails, the length b was set such that $b_{head,head} = b_{head,tail} = 0.95\delta$ and $b_{tail,tail} = 1.0\delta$. δ and ε thus set the length and energy scales of the simulation. In this implicit solvent model, the bilayer is held together by long-range attractive potentials between all tail beads and no water molecules are present in the simulation. Even in the absence of solvent, the long-range potential was shown by the authors of the model to self-assemble free lipids into a bilayer that displays physical parameters (*e.g.* area per lipid, bending modulus, *etc.*) equivalent to those found in biological membranes.[35,36] The chief advantage of the solvent-free approach is computational efficiency, even compared to other coarse-grained models.[38] For this long-range interaction we used a modified Lennard-Jones potential,

$$U_{attr}(r) = \begin{cases} -\varepsilon & r < r_c + w_f \\ 4\varepsilon\left[\left(\dfrac{b}{r - w_f}\right)^{12} - \left(\dfrac{b}{r - w_f}\right)^{6}\right] & r_c + w_f \leq r \leq 3.0\delta \\ 0 & r > 3.0\delta \end{cases} \tag{3}$$

Together, the combination of eqn (2) and eqn (3) give a Lennard-Jones potential modified by the addition of a flat plateau inserted at the energy minimum, ε, with a width w_f. Cooke *et al.* showed that changing the value of w_f changed the bilayer state from fluid to gel phase and is a critical tuning parameter in this model. In this work, w_f was set to 0.35δ, corresponding to a fluid bilayer according to the phase diagrams in ref. 36. The length scale of the system was set as $\delta = 0.7$nm in order to reproduce experimental measurements for the average area per lipid in the fluid phase. Finally, the energy scale was set by $\varepsilon = 1.3k_BT$, again consistent with these phase diagrams. With this set of potentials, the bilayer self-assembled from a random initial lipid configuration. Fig. 2 presents a schematic of the potentials present in the system, with additional details available in ref. 36.

The NP was constructed as a uniformly spherical hollow shell of beads, assembled by defining an initial icosahedron and iteratively bisecting sides of each face, then scaling each bead to the appropriate radius to yield a spherical surface. Based on this assembly method, all surface beads had six nearest neighbors except for the initial twelve beads which had five nearest neighbors, creating a well-defined lattice. All beads on the NP surface had a diameter of δ and the diameter of the assembled particle was set to 14.0δ, or 9.8 nm, with 642 total beads. The spherical surface was maintained by joining all beads together with harmonic springs to maintain their initial positions. Finally, each bead on the surface was defined as either hydrophobic or hydrophilic with a set phase fraction ϕ defining the relative proportions of each type.

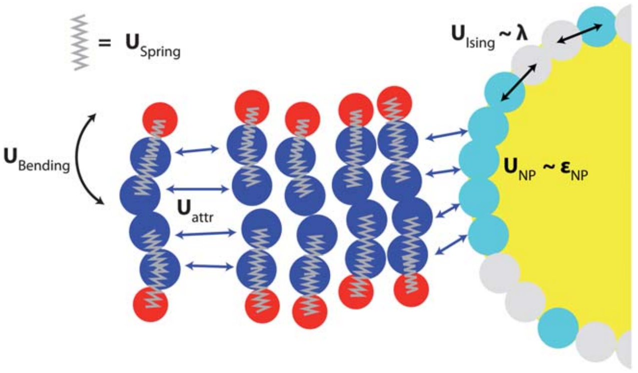

Fig. 2 Schematic illustrating different potentials acting on the system. The bilayer was held together by a combination of long-range attractive, bending, and spring potentials as described by ref. 36. The NP interacts with the bilayer *via* short-ranged attractive and repulsive potentials. Rearrangement of beads on the surface was governed by the Ising model with key parameter λ.

Interactions between the NP and bilayer were modeled using a combination of long- and short-ranged potentials. The long-range potential described in eqn (3) was applied between hydrophobic beads on the NP surface and the lipid hydrophobic tails; however, this potential was only applied when the NP beads were not within the core of the bilayer (defined as the z-coordinate of the NP bead being within the z-coordinates of the upper and lower head beads of the closest lipids). Once NP beads were embedded in the bilayer, however, a repulsive short-ranged potential was applied between embedded hydrophilic NP beads and the bilayer core, while an attractive short-ranged potential was applied between hydrophobic NP beads and the bilayer core. The short-ranged potentials were given by

$$U^{np}_{attr}(r) = -\varepsilon_{np}e^{-r/\xi} \tag{4}$$

$$U^{np}_{rep}(r) = \kappa_{np}e^{-r/\xi} \tag{5}$$

where ε_{np} and κ_{np} are prefactors giving the strength of the attractive and repulsive potentials, respectively, and ξ is the decay length. The short-range potentials were necessary to realistically model the system because the long-range potential alone presented no barrier for moving hydrophilic NP beads into the bilayer core, biasing lipids toward completely wrapping around the NP. Using the short-range potentials encouraged strong hydrophobic matching between hydrophobic beads on the NP and the lipid tails, while the repulsive short-ranged potential modeled the cost for moving hydrophilic beads into the core and explicitly penalized unphysical conformations. These potentials thus can be thought of as modeling the interfacial energy between the NP and bilayer. The long-range attractive potential modeled the driving force for hydrophobic attraction (*i.e.* the hydrophobic effect[39]) and provided an initial driving force for NP-bilayer interaction until the NP came into contact with the bilayer core. For all simulations κ_{np} was fixed at $1.0\,k_bT$, while ε_{np} was varied as a primary tuning parameter. Though the value of

κ_{np} was low, this was sufficient to ensure favorable rearrangement of the surface to avoid hydrophilic NP-hydrophobic tail bead contacts for all observed simulations (with the rearrangement process detailed below), and higher values of κ_{np} made no appreciable difference. ξ was set such that the attractive potential dropped to a value of $0.1k_BT$ at a distance of two bead diameters, ensuring that both potentials were very short-ranged. Though there was a jump in the potential felt by the NP surface when there was a switch from the long- to short-ranged potentials upon NP insertion, this jump had little effect on final simulation results since the strength of the short-ranged potentials primarily controlled NP-bilayer behavior. Finally, it should be noted that no interactions with the hydrophilic lipid head beads were included; while in principle the NP could interact with the lipid heads (as is observed in biological systems, including cell-penetrating peptides[4]), these interactions would likely have a highly specific form depending on the specific structure of the NP surface that is not within the context of this simple model and will be considered explicitly in future work. However, at the phenomenological level we can think of these interactions as essentially modifying the effective surface tension, and thus are incorporated within this coarse-grained model in the constants κ_{np} and ε_{np}.

Two separate simulation methodologies were employed to simultaneously model the evolution of bead positions in the system and dynamic rearrangement of the NP surface. A Brownian dynamics algorithm was used to simulate the motion of beads in the bilayer system subject to the potentials described above. Brownian dynamics is a simulation technique developed to implicitly model the effect of solvent by incorporating random forces that generate Brownian motion. This simulation technique is particularly appropriate for this model given the lack of explicit solvent molecules in the coarse-grained representation of the bilayer and NP. The algorithm for Brownian dynamics is:[40]

$$\mathbf{r}(t+\Delta t) = \mathbf{r}(t) + \frac{D}{k_B T}\mathbf{f}(t)\Delta t + \Delta\mathbf{r}^G \tag{6}$$

where D is the diffusion coefficient, Δt is the step size over which the forces $\mathbf{f}(t)$ are assumed to be constant, and $\Delta\mathbf{r}^G$ is a random force with each component chosen independently from a Gaussian distribution with a mean of zero and a variance of $2D\Delta t$. Forces are calculated directly from the potentials described above during each timestep. This equation can be simplified to dimensionless units by defining $\tilde{\mathbf{r}} = \mathbf{r}/\delta$, $\tilde{\mathbf{f}} = \mathbf{f}\delta/kT$, and $\tilde{\Delta}t = \Delta t/\tau$ where τ is the characteristic diffusion time, given by $\tau \approx \langle\delta^2\rangle/D$. Fluctuation-dissipation theory also allows the random force to be written as

$$\Delta\mathbf{r}^G = \sqrt{\frac{2D}{\Delta t}}\Delta\tilde{\mathbf{r}}^G \tag{7}$$

Substituting in these relations reduces eqn (6) to the dimensionless form

$$\tilde{\mathbf{r}}(t+\Delta\tilde{t}) = \tilde{\mathbf{r}}(t) + \Delta\tilde{t}\tilde{\mathbf{f}}(t) + \sqrt{2\Delta\tilde{t}}\Delta\tilde{\mathbf{r}}^G \tag{8}$$

Eqn (8) was used to model bead motions in the system with dimensionless step size $\Delta\tilde{t} = 10^{-4}$.

To model the rearrangement of the NP surface, a Monte Carlo algorithm was used to switch adjacent beads on the NP surface to maintain an optimal configuration. For each Monte Carlo timestep, two near-neighbor beads of opposite type (hydrophobic/hydrophilic) were chosen and randomly switched with a probability

$$P_{ij} = \begin{cases} 1 & \Delta U_{ij}^{ising} < 0 \\ e^{-\Delta U_{ij}^{ising}/kT} & \Delta U_{ij}^{ising} \geq 0 \end{cases}$$

where ΔU_{ij}^{ising} is the change in energy of beads i and j and their neighbors from the Ising model defined in eqn (1). The external field B_i in this equation was determined for each ligand from the pair-potentials defined in eqn (3), (4) and (5) based on the current positions of the beads as determined by Brownian dynamics. By explicitly switching beads, the total number of each type of ligand on the NP surface was conserved throughout the entire simulation run. As a model simplification, the timescale for rearrangement was assumed to be faster than the diffusion time of lipids. This simplification maintains generality by ignoring the specific mechanism, and hence timescale, of rearrangement for the NP surface (see Sec. 6 for examples of possible rearrangement mechanisms). Given the assumption of fast rearrangement, 1 000 Monte Carlo timesteps were taken per Brownian dynamics timestep. During the entire simulation run, then, the NP surface was continuously rearranged such that the positions of the NP beads always minimized the surface energy given by eqn (1). From this equation and the potentials that determine B_i, rearrangement was dependent on the parameter λ, the cost for neighbor interactions on the surface, κ_{np}, the cost for exposing hydrophilic NP beads to lipid tails, and ε_{np}, the gain in energy for bringing hydrophobic NP beads in contact with lipid tails. It can be said that this methodology models a fast-responsive NP. The opposite regime, in which the NP cannot rearrange rapidly and maintains a fixed surface morphology, has been studied previously[16,19,21,23] and will not be addressed in the present study.

To calculate the critical value λ_c for the ODT, Monte Carlo simulations of the rearrangement process alone were run in the absence of a bilayer with steadily increasing values of λ. The total system energy was calculated from eqn (1), where the energy was summed over the entire surface and the perturbing field B_i was set to 0 for all beads since no bilayer was present. The heat capacity of the system is proportional to the fluctuations in the surface energy and was also calculated as a function of λ.[41] λ_c was identified as the value of λ where a spike in the heat capacity was observed, which occurred for a value of 0.32 for a phase fraction of $\phi = 0.5$ and 0.38 for $\phi = 0.4$ and $\phi = 0.6$.

Full simulations were run by introducing NPs very close to the surface of pre-equilibrated bilayers in the fluid state containing 7 200 lipids. The bilayer was maintained with zero surface tension by using large free bilayers (*i.e.* no periodic boundary conditions). No additional driving force for aggregation was introduced. Simulations were run for 40 million Brownian dynamics timesteps. Three parameters were varied between simulations: λ, ε_{np}, and ϕ.

3 Simulation results and discussion

Fig. 3 presents simulation snapshots of the observed NP-bilayer interactions and corresponding "phase diagrams" for the system, depicting values of λ and ε_{np} for which the different behaviors were observed. Three diagrams are shown, denoting observed system behavior as a function of the phase fraction ϕ of NP hydrophilic beads. λ is normalized by the critical value λ_c for each ϕ. If $\lambda/\lambda_c < 1$, the NP surface preferred a homogeneous state when not in contact with the bilayer, while if $\lambda/\lambda_c > 1$ the NP surface preferred a phase separated state when not in contact with the bilayer. ε_{np} controls the strength of the interaction between lipids and the hydrophobic beads on the NP surface; higher values of ε_{np} corresponds to stronger attraction. Surface rearrangement was also critically dependent on ε_{np} since the parameter B_i in eqn (1) is determined by NP-bilayer contact and hence the value of ε_{np}.

Varying λ and ε_{np} gave rise to five distinct behaviors that are illustrated in Fig. 3a. The first behavior (black diamonds in Fig. 3) was trivial. For low values of ε_{np} and low values of λ, the surface of the NP maintained an homogeneous morphology since the value of ε_{np} was too small to induce surface reconstruction on the NP - that is, even when in contact with the bilayer the morphology was dominated by the parameter λ rather than the field B_i. The repulsive interactions between the hydrophobic bilayer core and the hydrophilic ligands in the homogeneous morphology thus prevented any NP-bilayer complexation. In the case of $\lambda/\lambda_c > 1$, where the NP assumed a Janus morphology, if ε_{np} was too low there would be an insufficient driving force for penetration to compensate for the cost in deforming the bilayer. The other four regimes all involved perturbation of the bilayer, and were distinguished largely by the NP's ability to rearrange its surface to maximize favorable interactions between the surface and the bilayer core. Note that in all cases, NP-bilayer interactions occurred spontaneously since no additional force was applied to push the NP into the bilayer.

For values of $\lambda < \lambda_c$ and low values of ε_{np}, a weak complexation behavior was observed (red circles in Fig. 3). The NP was unable to translocate to the bilayer midplane but instead induced significant curvature of the bilayer, similar to the curvature induced by wedge-like proteins.[42] This behavior resulted from the strong tendency for the NP to maintain a homogeneous surface when $\lambda < \lambda_c$, and the relatively weak interaction with the bilayer was insufficient to induce surface reconstruction for more favorable hydrophobic matching. The overall driving force for penetration was thus insufficient to allow complete penetration to the midplane, and the bilayer instead curved to maximize matching with the curved surface of the sphere.

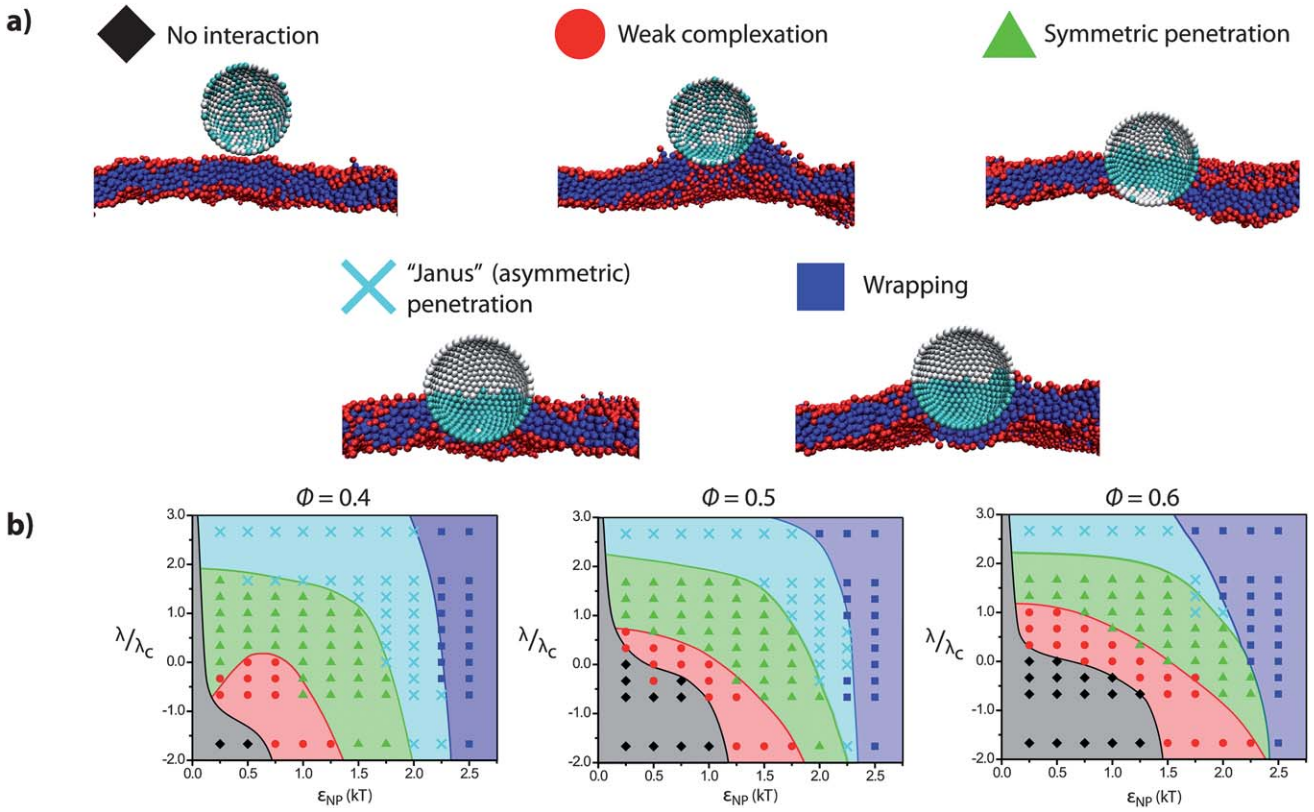

Fig. 3 Results from coarse-grained Brownian dynamics simulations with NP of diameter $2R \approx 14.0\delta$. The NP surface dynamically rearranges to minimize the surface energy *via* a Monte Carlo algorithm coupled to the positions of beads in the Brownian dynamics simulation. Values of the Ising parameter λ are shown scaled by the critical value λ_c, which was 0.32 for a hydrophilic phase fraction $\phi = 0.5$, and 0.38 for $\phi = 0.4$ or $\phi = 0.6$. **a)** Simulation snapshots of the five observed behaviors, including the case when no interaction between NP and bilayer was observed. Each behavior is described in detail in the text. Teal beads on the NP are hydrophobic, white beads are hydrophilic. Note especially the three-region symmetric surface morphology in the case of penetration. The distinction between "Janus" penetration and wrapping is evident from the lack of lipids coordinating the bottom surface of the NP in the "Janus" case, leaving the hydrophobic cap exposed to solvent. **b)** Phase diagrams illustrating when each different behavior was observed as a function of the key parameters λ, ε_{np}, and ϕ. Note the colors and symbols correspond to the representative snapshots in a).

When λ or ε_{np} was increased, the NP surface was able to rearrange to form a characteristic three-region symmetric morphology and the NP penetrated fully to the bilayer midplane (green triangles in Fig. 3). The region of the NP that was embedded in the bilayer core was primarily hydrophobic and the two protruding spherical caps were hydrophilic. This morphology resembled typical transmembrane proteins, which exhibit surfaces with large hydrophobic regions confined to the bilayer core and hydrophilic regions located in solvent. The formation of this surface resulted from both a low barrier to rearrangement and strong perturbation from the bilayer (high ε_{np}). The barrier for formation of this surface morphology was lowest when λ was near the critical value λ_c for an ODT on the particle surface. Near this transition, the energy cost for an initially homogeneous surface to phase separate was low, and the cost for an initially heterogeneous surface to create a third phase (and resulting line tension) was also low. The perturbing effect of the bilayer due to ε_{np} was thus able to induce the rearrangement of hydrophobic ligands into contact with the bilayer core while displacing hydrophilic ligands at the same time, leading to a strongly preferred transmembrane morphology. A simulation snapshot of this three-region symmetric morphology is shown in Fig. 3a.

If λ was further increased well above λ_c, the NP surface strongly preferred a phase separated, Janus morphology (shown in Fig. 1a) in the absence of the bilayer. As a result, contact with the bilayer was insufficient to induce the three-region symmetric morphology characteristic of penetration due to the high line tension between phases on the surface. There were two separate behaviors that were observed in this case. For low values of ε_{np}, the favorable interaction between lipids and the hydrophobic region of the NP surface led to some anchoring of lipids to the surface (teal crosses in Fig. 3). However, the bilayer did not show noticeable deformation, with the lipids preferring to maintain coordination by other lipids. In this case, the NP exposed the hydrophobic ligands not in contact with the bilayer core to the implicit solvent while still penetrating toward the bilayer midplane, a mechanism we refer to as "Janus" penetration. It is likely that strongly Janus particles of this type would have induced pore formation in order to minimize this hydrophobic exposure if multiple NPs were present in the simulation.[22,37] For large values of ε_{np}, lipids instead anchored strongly to the NP surface and wrapped around the entire hydrophobic region of the NP (blue squares in Fig. 3). The favorable gain in energy due to a high ε_{np} from these NP-lipid contacts was sufficient to overcome the considerable strain energy associated with this bilayer disruption. NP adhesion of this type has been observed in simulation studies previously, and is well-studied.[43]

The phase diagrams for different hydrophilic phase fractions showed the same five behaviors though under different parameters. As ϕ increased from 0.4 to 0.6, symmetric penetration behavior was observed for a smaller range of λ and ε_{np} values, consistent with a smaller number of hydrophobic ligands and resulting decrease in attractive interactions with the bilayer. Most notable, however, is that symmetric penetration behavior was consistently observed for the lowest values of ε_{np} when the NP surface was near an ODT ($\lambda/\lambda_c \approx 1.0$), implying that even if the gain in interfacial energy was minimal the NP was still able to penetrate. This result can be again understood due to the low cost of forming the three-region symmetric morphology exhibited by NPs that penetrate.

These phase diagrams present several options for manipulating NP-bilayer interactions depending on the ease of modifying the key parameters λ, ε_{np}, and ϕ. In principle, λ is dependent on the physical system under consideration, some of which are discussed in Sec. 6. Since ε_{np} is effectively an interfacial energy, this parameter may be more difficult to modify chemically, and hence NP-bilayer behaviors should be tuned by modifying λ and ϕ.

4 Theory

While the coarse-grained simulations established the variety of interactions possible between the NP and bilayer, the thermodynamics of NP penetration are of particular interest, as this is the behavior most suitable for biological applications. The simulation results indicated that two primary types of penetration were possible: symmetric penetration, where the NP translocated to a stable position at the bilayer midplane and all hydrophobic surface area was exposed to the bilayer core; and Janus penetration, where the NP maintained a phase separated Janus morphology and exposed some hydrophobic area to solvent upon penetration into the bilayer. These two behaviors were observed for relatively similar values of ε_{np}, but different values of λ, with Janus penetration preferred when $\lambda/\lambda_c > 1$. To fully understand the penetration of NPs, then, the free energy change for achieving either of these two states was calculated, with the lower free energy state being preferred at equilibrium. In this section, the change in free energy of the system for both cases will be derived using a continuum approximation for the NP and bilayer in place of the discretized approach used in simulations. In the continuum approximation, the key parameter ε_{np}, which acted as a pair-potential in simulations, is replaced instead by γ, a parameter giving the attractive interfacial energy per hydrophobic ligand. Similarly, κ_{np}, the prefactor for the repulsive interaction that was fixed in the simulations is now replaced by μ, the repulsive interfacial energy per hydrophilic ligand. The free energy is thus a function of γ, μ, and λ. Finally, while λ in this continuum approximation is qualitatively the same as in the discretized simulations, treating the NP as a continuum rather than discrete lattice leads to a quantitatively different λ_c than in simulations; however, the effect of λ on the system remains the same.

The approach for calculating the free energy change for both the symmetric and Janus penetrated states is similar, so the analysis will first be performed for the symmetric case. Relevant differences for Janus penetration are then discussed in section 4.7. Fig. 4 is a simple schematic outlining the system under consideration in the case of symmetric penetration. The initial state of the system is an unperturbed bilayer of height h_0 and a NP of radius R, with a surface morphology dependent on the neighbor interaction energy λ. It is assumed that in the final state the NP penetrates exactly to the bilayer midplane, and there is complete symmetry around the bilayer center. It is further assumed that the NP surface will divide into two distinct regions, representing one area exposed to the bilayer core and one area (divided into two spherical caps) exposed to aqueous solvent. These regions are labeled as A_+ and A_- in Fig. 4, and can be calculated from R and h, the deformed thickness of the bilayer. In

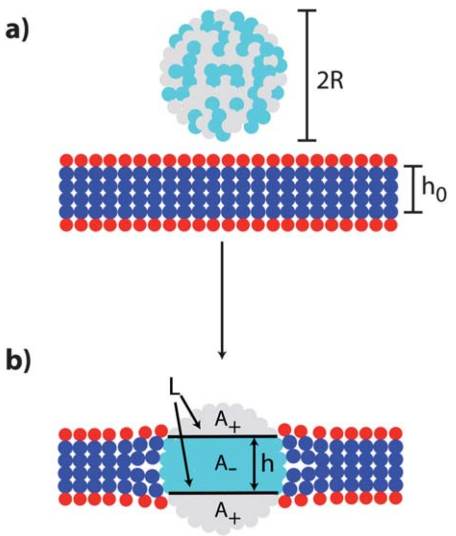

Fig. 4 Schematic illustrating the different geometric variables considered in theory. **a)** The initial state, with a NP of radius R with either a phase separated or homogeneous surface (drawn here as homogeneous) dependent on λ. The unperturbed bilayer has thickness h_0. **b)** The final state, with a NP exhibiting phase separation to maximize hydrophobic matching, leading to two regions of identical area A_+ by symmetry outside the bilayer, and region exposed to the bilayer interior with area A_-. The dividing line between the two phases has circumference L, and the bilayer assumes a new thickness h.

general, the region labeled as A_+ will tend to be more hydrophilic due to solvent exposure, while the region labeled as A_- will tend to be more hydrophobic providing favorable hydrophobic matching. This morphology is identical to the surface morphology observed in simulations (shown in Fig. 3) when penetration occurs. Finally, the boundary between the external and internal regions on the surface has length L, and gives rise to a line tension between these two phases.

Based on the system described, four terms are included in the overall free energy change: $\Delta F_{int}(h, R, \gamma, \mu)$, the interfacial energy change for the NP surface; $\Delta F_{line}(h, R, \lambda)$, the line tension between regions on the NP surface; $\Delta F_{surf}(h, R, \lambda)$, the change in surface energy due to neighbor interactions; and $\Delta F_{bilayer}(h, h_0)$, the change in bilayer elastic energy from deformation induced by the particle. The total change in free energy is then:

$$\Delta F = \Delta F_{int} + \Delta F_{line} + \Delta F_{surf} + \Delta F_{bilayer} \qquad (9)$$

The driving force behind penetration is the change in interfacial energy, as all the other terms are positive. In what follows we will first calculate ΔF_{sym}, the total change in free energy for penetration to the symmetric state following from eqn (9). In section 4.7 the changes necessary to calculate ΔF_{Janus}, the total change in free energy for penetration to the Janus state, will be outlined, again following from eqn (9).

4.1 Surface (Ising) energy

The energy of the NP surface can be determined from the Ising model defined in eqn (1). In the simulations the Ising energy of the surface was explicitly calculated based on pair interactions; however, this calculation can be simplified using a mean-field approximation, where it is assumed that all the ligands in a given region have the same average "hydrophilicity." The two different regions, A_+ and A_- will generally have different average hydrophilicities, denoted by $\langle\sigma\rangle_+$ and $\langle\sigma\rangle_-$ respectively. Recall that in eqn (1), hydrophilic ligands are given a spin of +1 and hydrophobic ligands are given a spin of −1, so that the names of the two areas reflect the sign of the average hydrophilicity in each.

In this mean-field approximation, the summation in eqn (1) is replaced by

$$E_i = -\lambda\langle\sigma(\lambda)\rangle^2 \qquad (10)$$

Note that there is no reference to the number of neighbors for molecule i, as it is assumed that the number of near-neighbors is incorporated in the effective parameter λ. The external field B_i is also set to zero; the effect of the external field from the bilayer core is included in the ΔF_{int} term described below. Given these assumptions, a complete expression for the surface energy is written as

$$E_{surf} = -\rho\lambda(A_+\langle\sigma\rangle_+^2 + A_-\langle\sigma\rangle_-^2) \qquad (11)$$

where ρ is the grafting density of ligands on the surface. In addition to the surface energy, it is also necessary to include the Bragg-Williams entropy of mixing in each region under the assumption that the rearrangement mechanism gives rise to a configurational entropy:

$$S_- = -k_B\rho A_-[\phi_-\ln(\phi_-) + (1-\phi_-)\ln(1-\phi_-)] \qquad (12)$$

$$S_+ = -k_B\rho A_+[\phi_+\ln(\phi_+) + (1-\phi_+)\ln(1-\phi_+)] \qquad (13)$$

where $\phi_- = \dfrac{1+\langle\sigma\rangle_-}{2}$ and $\phi_+ = \dfrac{1+\langle\sigma\rangle_+}{2}$, representing the phase fractions of hydrophilic ligands in each region, rather than the average hydrophilicity, and k_b is the Boltzmann constant. Note that the entropy of either region is simply set to 0 if either ϕ is 0, as this is the limit of complete phase separation.

The total surface free energy is then given as the sum of the energetic and entropic components, giving:

$$F_{surf}^{final} = E_{surf} - T(S_- + S_+) \qquad (14)$$

Note that while this is the final surface free energy, the free energy change ΔF_{surf} is the important quantity, so the baseline free energy must also be calculated as described in section 4.3.

4.2 Line tension

If the average hydrophilicities of A_+ and A_- are different, as is expected in general, a line tension will arise due to unfavorable interactions along the boundary between regions. This term can be calculated from the Ising model and eqn (10) by assuming that ligands on the border between the regions have an environment where half of the neighbors are from one region and half are from the other. Along the boundary, the surface energy of the ligands inside the bilayer will be given by $-\dfrac{\lambda}{2}\left[\langle\sigma\rangle_-\langle\sigma\rangle_+ + \langle\sigma\rangle_-^2\right]$, while the energy of the ligands outside the bilayer will be given by $-\dfrac{\lambda}{2}\left[\langle\sigma\rangle_-\langle\sigma\rangle_+ + \langle\sigma\rangle_+^2\right]$. However, in the previous section it was assumed that all ligands had the same surface energy, so to avoid overcounting $-\lambda\langle\sigma\rangle_-^2$ must be subtracted for each ligand along the boundary internal to the bilayer and $-\lambda\langle\sigma\rangle_+^2$ must be subtracted for each ligand external to the bilayer since these energies would have been already been included in the previous calculation. Finally, it is necessary to account for the number of ligands affected, which is approximately given by the product of the boundary length L and $\sqrt{\rho}$. The total line tension (doubled to account for the two boundaries) is then:

$$F_{line}^{final} = \lambda L\sqrt{\rho}\left[\langle\sigma\rangle_-^2 + \langle\sigma\rangle_+^2 - 2\langle\sigma\rangle_-\langle\sigma\rangle_+\right] \qquad (15)$$

Given the assumption of spherical symmetry, the boundary length is solved as the circumference of a spherical cap, yielding $L = \pi\sqrt{4R^2 - h^2}$. As with the surface energy, this expression is for the final line tension only and must be compared to the baseline line tension to find ΔF_{line}.

4.3 Baseline surface energy and line tension

In order to calculate the free energy change upon bilayer complexation, the baseline energy of the NP surface must be determined as the sum of a line tension and surface energy term with equations similar to those described above. It is assumed that the NP surface is divided into at most two phases (corresponding to a Janus particle), and that the surface energy and line tension can be calculated in terms of A_1, the area of one of these two phases, and $\langle\sigma\rangle_1$, the average hydrophilicity of this phase. Numerically minimizing the sum of the surface energy and line tension for a given λ yields A_1, $\langle\sigma\rangle_1$, and the baseline free energy. Below λ_c, the energy will be minimized when $A_1 = 0$, implying only a single, homogeneous surface, while above λ_c, $A_1 > 0$ implying phase separation. The critical λ_c marking the ODT thus corresponds to the lowest λ where A_1 is greater than 0. Using this method, λ_c was found to be invariant as a function of R, and was equal to 0.59 for $\phi = 0.5$ and 0.71 for $\phi = 0.4$ and $\phi = 0.6$.

4.4 Bilayer deformation

The NP-bilayer interaction could lead to deformations of the bilayer away from its unperturbed thickness in order to gain in interfacial energy. As a simple estimate of this deformation energy, we used a continuum model developed by Nielsen and Anderson[44,45] that predicts the change in bilayer deformation energy due to thickness deformations. The model has been previously parameterized to match experimental results from the interactions between bilayers and transmembrane gramicidin channels, which have approximately the same size as the NPs under consideration and hence make a suitable analogue. Finally, the authors of this model also demonstrated that the effect of surface tension was minimal and can be ignored, an assumption also made in this work. Based on their work and the choice of suitable fitting parameters the deformation free energy, assuming a baseline of no perturbation, is written as

$$\Delta F_{bilayer} = \left[278.0\left(\frac{R}{3.0}\right)^{1.023} + 77.0\right]\left(\frac{h - h_0}{2}\right)^2 \qquad (16)$$

4.5 Interfacial energy

The final free energy change to consider is the interfacial energy of the system, reflecting the free energy change associated with changing the solvent conditions around each ligand. This free energy change can be calculated in terms of the penalty incurred by the exposure of ligands to unfavorable solvent conditions. Hydrophobic ligands exposed to aqueous solvent are penalized by the parameter γ, while hydrophilic ligands exposed to the hydrophobic bilayer core are penalized by the parameter μ. The driving force for aggregation is the minimization of the interfacial energy, since in the baseline state the hydrophobic ligands are necessarily exposed to aqueous solvent in this model and incur an energy penalty.

We can write the initial interfacial energy of the initial NP in terms of the phase fraction of hydrophilic ligands alone, since in principle the interfacial energy does not depend on whether the surface is mixed or homogeneous. The baseline interfacial energy is

$$F_{int}^{baseline} = A\rho(1 - \phi)\gamma \qquad (17)$$

In analogous fashion, we can calculate the interfacial energy of the internal (hydrophobic) and external (hydrophilic) regions upon complexation, with the energy based on the average hydrophilicities of those regions.

$$F_{int}^{+} = \frac{A_+\rho(1 - \langle\sigma\rangle_+)\gamma}{2}$$

$$F_{int}^{-} = \frac{A_-\rho(1 + \langle\sigma\rangle_-)\mu}{2}$$

The total change in interfacial energy is then given as:

$$\Delta F_{int} = \frac{\rho}{2}\left[A_+(1 - \langle\sigma\rangle_+)\gamma + A_-(1 + \langle\sigma\rangle_-)\mu - 2A(1 - \phi)\gamma\right] \qquad (18)$$

4.6 Conservation relations

A key assumption made in this model is that the total number of hydrophobic and hydrophilic ligands is fixed, and hence is determined by the initial phase fraction ϕ of the system. Since the total area of the system is also fixed, $\langle\sigma\rangle_+$ and $\langle\sigma\rangle_-$ can be determined from a conservation condition related to the relative areas of the two regions and the initial phase fraction:

$$\frac{A_-}{A}\langle\sigma\rangle_- + \frac{A_+}{A}\langle\sigma\rangle_+ = 2\phi - 1 \qquad (19)$$

where A is the total surface area of the NP. Note that the different areas can be further simplified to functions of R and h by applying geometric identities for the area of a spherical zone (A_-) and spherical cap (A_+):

$$A_- = 2\pi Rh \qquad (20)$$

$$A_+ = 2\pi R(2R - h) \qquad (21)$$

$$A = 4\pi R^2 \qquad (22)$$

4.7 Janus penetration

When $\lambda/\lambda_c > 1$, the NP surface will tend to phase separate into a Janus state consistent with Fig. 1b. In this case, the NP may penetrate the bilayer by the "Janus penetration" mechanism identified in simulations rather than by the three-region symmetric penetration mechanism considered here. The Janus penetration mechanism is preferred at high λ because retaining a two- rather than three-region morphology reduces the line tension of the system, though at the cost of exposing more hydrophobic area to solvent. In this section the free energy change for Janus penetration, ΔF_{Janus}, will be calculated, which can then be compared to the free energy change for symmetric penetration discussed above to determine the dominant penetration mechanism as a function of γ and λ.

Fig. 5 illustrates the proposed final state of the system upon Janus penetration. As in Fig. 4, the NP surface is divided into three regions denoted as A_+, A_-^I, and A_-^E, corresponding to the area of predominantly hydrophilic ligands exposed to solvent, the area of predominantly hydrophobic ligands exposed to the bilayer core, and the area of predominantly hydrophobic ligands exposed to the solvent. It is no longer assumed that there is symmetry around the bilayer midplane so that $A_+ \neq A_-^E$; this allows both the bilayer thickness h and the thickness of the exposed hydrophilic region h^E to vary in order to minimize the free energy change. It is assumed that the average hydrophilicity $\langle\sigma\rangle_-$ is identical in both regions A_-^E and A_-^I.

Calculation of the free energy change for Janus penetration follows along the same lines as the previous calculation for symmetric penetration. The change in surface energy is identical to eqn (14), with the area $A_- = A_-^E + A_-^I$. The line tension is equal to 1/2 the value of eqn (15) since there are only two adjacent regions of differing hydrophilicity. Furthermore, the value L is now given by $L = 2\pi\sqrt{h^E(2R - h^E)}$ due to the new geometry of the system. The bilayer deformation term is assumed to be identical to eqn (16). In principle, the Janus penetration mechanism could involve additional deformation modes (such as bending or lipid tilt[46]) other than the thickness deformation assumed, but for simplicity the same expression is used. Finally, the interfacial energy must take into account that the region A_-^E is exposed to solvent; this gives a revised expression for the interfacial energy of

$$\Delta F_{int}^{Janus} = \frac{\rho}{2}\left[A_+\left(1 - \langle\sigma\rangle_+\right)\gamma + A_-^I\left(1 + \langle\sigma\rangle_-\right) + A_-^E\left(1 - \langle\sigma\rangle_-\right)\gamma - 2A(1 - \phi)\gamma\right] \quad (23)$$

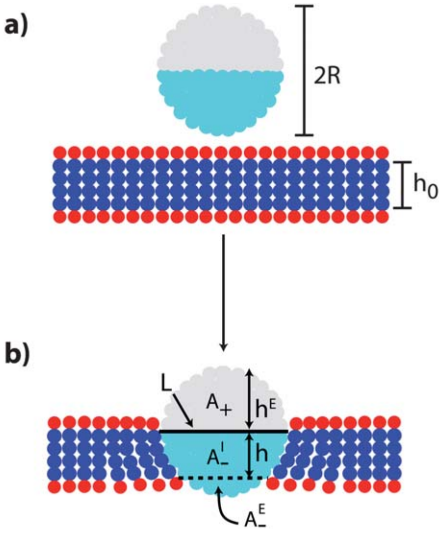

Fig. 5 Schematic illustrating the different geometric variables considered for Janus penetration. **a)** The initial state, with a NP of radius R in the phase separated Janus state. The unperturbed bilayer has thickness h_0. **b)** The final state, with a NP exhibiting phase separation and in contact with the bilayer. Unlike the symmetric penetrated state, the NP does not necessarily translocate to the midplane, leading to three regions of distinct areas A_+, A_-^I, and A_-^E. The thickness of the exposed hydrophilic region is given as h^E, while the thickness of the deformed membrane is h. Areas A_-^I and A_-^E have the same average hydrophilicity and hence there is no line tension at their interface, which is drawn with a dashed line. The dividing line between the two areas of different hydrophilicity, A_+ and A_-^I, has length L.

To complete the analysis of Janus penetration, the expression for the different areas must also be updated. Again calculating areas based on geometric formulas for spherical caps and zones yields

$$A_+ = 2\pi R h^E \quad (24)$$

$$A_-^I = 2\pi R h \quad (25)$$

$$A_-^E = 2\pi R(2R - h - h^E) \quad (26)$$

$$A = 4\pi R^2 \quad (27)$$

Finally, the conservation relation eqn (19) remains the same, with $A_- = A_-^E + A_-^I$.

5 Theory results and discussion

In the previous section, the free energy change for moving a NP from a fully solvated initial position outside of the bilayer to a position at the bilayer midplane was calculated as a function of R, h, γ, μ, ϕ and λ. Furthermore, the free energy change for Janus penetration was also calculated in terms of the same variables and the additional geometric variable $h^{E.}$ To compare with simulation results, the full free energy change for both cases was calculated for different values of γ (which is qualitatively analogous to ε_{np} in the simulations), λ, and ϕ. In each case, the free energy change was minimized as a function of h to find the perturbed bilayer thickness for each set of parameters. For Janus penetration, the free energy change was further minimized as a function of h^E, with h^E constrained to the range of $0 \leq h^E \leq 2R\phi$ to be consistent with the Janus morphology. The grafting density ρ was set to 4.77 ligands/nm^2, in accordance with the typical density of surface monolayers,[47] though in principle the grafting density could differ for other model systems.

Fig. 6 shows the result of calculating free energy changes for both symmetric and Janus penetration. In Fig. 6a, the change in free energy of each state is calculated for different values of ϕ with $R = 5nm$, while in Fig. 6b the change is shown as a function of R with $\phi = 0.5$. In both figures, the thick contour lines represent where $\Delta F = 0$ for either symmetric or Janus penetration; that is, to the right of the contours (higher γ) penetration is thermodynamically preferred, while to the left (lower γ) the free energy change for penetration is greater than zero and thus penetration is not expected. To distinguish whether symmetric or

Janus penetration is preferred, the dashed contour lines in both figures indicate where the free energy change between the two states is zero. Values of λ and γ above the dashed lines indicate where Janus penetration is preferred over symmetric penetration, while values of λ and γ below the dashed lines indicate where symmetric penetration is favorable over Janus penetration. Together, then, these contour lines can be compared to the simulation results to show where different forms of penetration are preferred under distinct conditions. Interpreting these results as a phase diagram for a single value of $R = 5nm$ and $\phi = 0.5$ is shown in Fig. 7. In this figure, the full contours for both Janus and symmetric penetration are drawn as red and yellow dashed lines respectively, with the black dashed line again indicating where the free energy change between the two penetrated states is zero. The different regions of the phase diagram are then colored according to the same scheme as Fig. 3 based on whichever penetrated state poses the largest free energy change from the baseline value. As in Fig. 3, black corresponds to no interaction, teal corresponds to Janus penetration, and green corresponds to symmetric penetration.

Fig. 6a shows that for all measured values of ϕ symmetric penetration behavior is observed for the lowest value of γ when $\lambda/\lambda_c \approx 1$, agreeing with simulation results. As λ increases above its critical value, Janus penetration is instead preferred, again agreeing with simulation results. The preference of Janus penetration at high λ is due to the increase in line tension as λ increases; the Janus state minimizes the line tension by only having two distinct regions rather than the three associated with symmetric penetration. Because the line tension is lowest near the ODT, symmetric penetration is still preferred for values of λ slightly higher than λ_c. If the NP surface slightly prefers mixing (*i.e.* λ is slightly lower than λ_c) then the change in surface energy required to separate the surface into three regions is similarly low near the ODT. In either case, then, the perturbation due to the bilayer, captured in the change in interfacial energy, is sufficient to induce the three regions associated with symmetric penetration. It is particularly interesting to note that although the

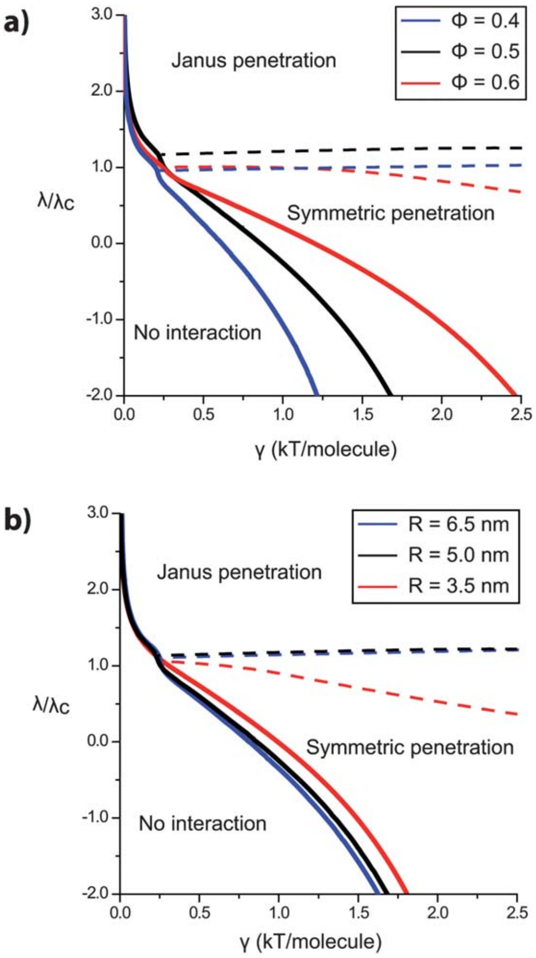

Fig. 6 Results from theoretical free energy minimization, with contour lines marking where the change in free energy from the free to translocated state is equal to 0. The surface energy parameter λ is scaled by the critical value λ_c for the ODT, which was equal to 0.59 for the hydrophilic phase fraction $\phi = 0.5$, 0.71 for $\phi = 0.6$ and $\phi = 0.4$, and did not change as a function of NP radius. The dashed contours indicate where the transition to Janus penetration is preferred over symmetric penetration. **a)** Contours for changing the hydrophilic phase fraction ϕ for fixed $R = 5nm$. For higher phase fractions, a greater interfacial energy γ is necessary for symmetric penetration, while Janus penetration remains highly favorable when $\lambda/\lambda_c > 1$. **b)** Contours for changing NP radius R for fixed $\phi = 0.5$. Penetration behavior is largely invariant as a function of NP radius, although for smaller radii Janus penetration is more favorable than symmetric penetration for larger values of γ.

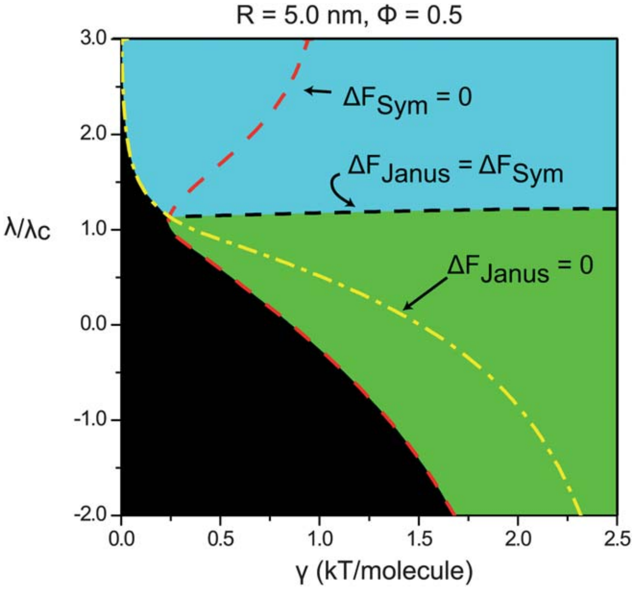

Fig. 7 Phase diagram interpretation of theoretical results. The yellow dot-dashed contour indicates where ΔF_{Janus}, the change in free energy from baseline to the Janus penetrated state, is equal to 0. To the right of this contour (*i.e.* higher γ) the Janus state is preferred over the baseline state. The dashed red contour indicates where ΔF_{sym}, the change in free energy from baseline to the symmetric penetrated state, is equal to 0. Finally, the dashed black contour indicates where the $\Delta F_{Janus} = \Delta F_{sym}$, indicating the transition between one penetrated state being preferred over the other. On the basis of these contours, the different regions are colored according to what state is thermodynamically preferred; black indicates no interaction, teal indicates Janus penetration, and green indicates symmetric penetration. This phase diagram can thus be directly compared to the phase diagram in Fig. 3.

contours for symmetric and Janus penetration vary significantly for different values of ϕ, symmetric penetration is always preferred for roughly the same values of γ near the critical point.

Fig. 6b shows the interesting result that the free energy change for penetration in either the symmetric or Janus state is roughly independent of NP diameter, again noting that in all cases studied the diameter is larger than the bilayer thickness. As in Fig. 6a, symmetric penetration is still observed for the lowest value of γ when λ is near the critical point. This result is relevant given the known size-dependence of endocytosis,[48] indicating that it may be possible to design NPs to penetrate non-specifically instead of achieving cellular uptake by endocytosis and then being trapped in endosomal compartments.

There are several discrepancies between the theoretical results and simulation results that bear discussion. First, a comparison of Fig. 3 and 6 a shows that in general the range of values of λ that prefer symmetric penetration is less broad in the theoretical results than in simulations. This difference can be attributed to the lack of fluctuations in the mean field theoretical model. However, both the theory and simulations do predict the important result that symmetric penetration is preferred for low values of γ or ε_{np} when $\lambda/\lambda_c \approx 1$. It should also be noted that at high ε_{np}, the simulations predict first Janus penetration then particle wrapping behavior as ε_{np} is increased, both results that are not obtained in the theory. The preference for Janus behavior at high ε_{np} can be attributed to kinetic trapping in the simulations. Because forming the three-region symmetric morphology necessarily relies on rearranging surface ligands across regions of the surface exposed to the bilayer core, at high values of ε_{np} the cost for moving hydrophilic ligands is prohibitively high, even if the final morphology is favored thermodynamically. It is probable that at long enough runtimes symmetric penetration would be observed in simulations even for large values of ε_{np}, but that is not observed in the simulations presented here. Wrapping is not considered in the theory because this would require incorporating single monolayer bending deformations into the continuum bilayer approximation which is beyond the scope of this study. Finally, the theory predicts that Janus penetration is observed even for $\gamma = 0$ if λ is sufficiently high, which is not indicated in Fig. 3. In simulations, it is observed that lipids tend to anchor to the curved NP surface, inducing a tilt deformation that comes at some small energetic cost that is not considered in the theory. This bilayer deformation would oppose penetration if the value of γ approaches zero, since then the driving force for penetration would also drop to zero. Again, these types of bilayer deformations are outside the scope of this study. Despite these differences between theory and simulations, overall the results agree well and show the same qualitative trends, particularly with respect to the preference for symmetric penetration near and below the ODT and Janus penetration above the ODT.

Combined with the simulation results, the theoretical analysis suggests that penetration may be highly tunable if λ can be varied experimentally, as will be discussed for model systems in the following section. Most important is the identification of symmetric penetration when the NP surface is near an ODT, since symmetric penetration mimics the morphology of transmembrane proteins and likely leads to stable NP complexation for long periods of time. Another interesting result is that the barrier for Janus penetration drops to nearly zero when $\lambda > \lambda_c$. This low barrier implies that Janus penetration may lead to stable pore formation when multiple NPs are present in order to further minimize exposed hydrophobic area.[22,37] Finally, it is important to note the relatively low magnitude of the interfacial energy γ necessary to achieve symmetric penetration when the surface is near a phase transition, providing a design goal for physical systems.

6 Model physical systems

Both simulations and theory demonstrate that bilayer penetration can be achieved if the NP surface is capable of rearranging, and that symmetric penetration, where the NP fuses with the bilayer in a manner similar to transmembrane proteins, is preferred when the NP surface is near an ODT. Several existing soft matter systems have been shown to exhibit the type of phase behavior assumed in this work, and hence may serve as model systems for environmentally-responsive NPs. A first example is gold NPs coated with a mixed hydrophilic/hydrophobic surface monolayer, which have been experimentally observed to penetrate bilayers.[8] Studies of this and similar systems have analyzed the phase characteristics of the monolayer as a function of chain length,[49,50] composition,[51,52] and temperature,[53] variables that could be captured in the effective parameter λ and can be modified experimentally. It also has been suggested that these systems exhibit lateral surface mobility, providing a mechanism for rearrangement consistent with this approach.[34,54,55] Finally, simulation studies of grafted gold NPs have also demonstrated that a great degree of asymmetry can result from ligand tilt alone,[47,56,57] which may effectively change the morphology of the surface, especially if biased by interaction with a preferential solvent.[58]

A similar system is NPs coated with mixed polymer brushes, rather than short chain alkane derivatives, yielding so-called "hairy" particles. In this system, λ is best represented by the Flory-Huggins interaction parameter χ, and experimental studies have already demonstrated the formation of different phases in either a Janus[59] or mixed morphology.[60,61] Polymer brushes can be designed to be stimuli-responsive, changing morphology as a result of exposure to different environmental conditions,[33] including changing solvent conditions, temperature, or pH. This imparts an ability to change surface morphology in connection to the results identified in this work, and experiments have demonstrated the ability to translocate stimuli-responsive particles across a hydrophilic-hydrophobic interface.[62–65] In addition, the NP core need not be gold, as triblock copolymers can form structures with similar morphologies.[66,67]

Finally, while these two classes of NPs are probably most suitable for further study related to this work given their extensive usage in current research, several other systems may exhibit translocation behavior. For instance, polymerosomes have recently been assembled that undergo a phase transition in the corona,[68] a process which affected cell uptake. It is possible that varying polymer composition to effect favorable interactions with the bilayer core could be used to drive non-specific translocation as described here. Another interesting system is a NP coated in an amphiphilic monolayer derived from V-shaped polymers,[69,70] which would maintain a fixed ratio of hydrophobic/hydrophilic ligands and could exhibit surface rearrangement.

7 Conclusions

In this work, we have shown that a NP with an environmentally-responsive mixed hydrophobic/hydrophilic surface can non-specifically penetrate to the midplane of a lipid bilayer. Penetration depends on the NP rearranging its surface to maximize favorable hydrophobic interactions while minimizing the exposure of hydrophilic ligands to the bilayer interior. The NP-bilayer interactions were studied *via* both coarse-grained Brownian dynamics simulations and continuum theory. We used a simple Ising model to characterize the dynamic rearrangement of the NP surface, and found that the key parameter that governs penetration is λ, the interaction energy between neighboring ligands on the NP surface. When λ is near λ_c, the critical value for an ODT, both theory and simulation predict that the NP will translocate to the bilayer midplane even for small values of γ, the hydrophobic interfacial energy per ligand. During this type of symmetric penetration, the NP surface rearranges to form a single band of hydrophobic ligands exposed to the bilayer hydrophobic core and two caps of hydrophilic ligands exposed to solvent, forming a stable morphology similar to transmembrane proteins. If λ is above λ_c, a Janus morphology is instead preferred on the NP surface that also leads to penetration, though at the cost of leaving hydrophobic ligands exposed to solvent. This state may lead to pore formation if multiple NPs are present. From simulations, several other non-specific NP-bilayer interactions were also identified depending on the relative competition between the cost of ordering the surface and the gain in interfacial energy. The theory further predicts that if $\lambda/\lambda_c \approx 1$, then symmetric penetration would be observed for small values of γ independent of NP radius.

On the basis of these results, it is clear that the parameter λ and its critical value λ_c are crucial in determining penetration behavior. In principle, both λ and λ_c can be determined independently of bilayer interactions as they are a function of the NP surface composition and environment alone. This work suggests that several well-studied soft matter systems with known phase behavior may serve as suitable experimental analogues for the NPs discussed. Furthermore, the theory suggests that NP-bilayer interactions may be highly tunable based on modifying λ, which in general may be a function of environmental conditions like pH or temperature depending on the specific system studied. Penetration behavior also depends on the interfacial energy γ; while this parameter may be more difficult to modify experimentally, near the ODT these results indicate that only a minimal value of γ is sufficient to drive symmetric penetration. These results thus suggest guidelines for the design of environmentally-responsive NPs that can complex with lipid bilayers by utilizing systems with known phase behavior.

Acknowledgements

This material is based on work supported under a National Science Foundation Graduate Research Fellowship. This work was also supported in part by the MRSEC Program of the National Science Foundation under award number DMR-0819762. Some of the computations in this paper were run on the Odyssey cluster supported by the FAS Sciences Division Research Computing Group.

References

1 S. J. Marrink and H. J. C. Berendsen, *J. Phys. Chem.*, 1996, **100**, 16729–16738.
2 S. J. Marrink and H. J. C. Berendsen, *J. Phys. Chem.*, 1994, **98**, 4155–4168.
3 M. Orsi, W. E. Sanderson and J. W. Essex, *J. Phys. Chem. B*, 2009, **113**, 12019–12029.
4 H. D. Herce and A. E. Garcia, *J. Biol. Phys.*, 2007, **33**, 345–356.
5 M. C. Morris, S. Deshayes, F. Heitz and G. Divita, *Biol. Cell*, 2008, **100**, 201–217.
6 A. E. Nel, L. Madler, D. Velegol, T. Xia, E. M. V. Hoek, P. Somasundaran, F. Klaessig, V. Castranova and M. Thompson, *Nat. Mater.*, 2009, **8**, 543–557.
7 S. Mitragotri and J. Lahann, *Nat. Mater.*, 2009, **8**, 15–23.
8 A. Verma, O. Uzun, Y. H. Hu, Y. Hu, H. S. Han, N. Watson, S. L. Chen, D. J. Irvine and F. Stellacci, *Nat. Mater.*, 2008, **7**, 588–595.
9 O. Uzun, Y. Hu, A. Verma, S. Chen, A. Centrone and F. Stellacci, *Chem. Commun.*, 2008, 196–198.
10 T. Hessa, H. Kim, K. Bihlmaier, C. Lundin, J. Boekel, H. Andersson, I. Nilsson, S. H. White and G. von Heijne, *Nature*, 2005, **433**, 377–381.
11 T. Hessa, N. M. Meindl-Beinker, A. Bernsel, H. Kim, Y. Sato, M. Lerch-Bader, I. Nilsson, S. H. White and G. von Heijne, *Nature*, 2007, **450**, 1126–1130.
12 T. W. Allen and S. Dorairaj, *Proc. Natl. Acad. Sci. U. S. A.*, 2007, **104**, 4943–4948.
13 H. Lee and R. G. Larson, *Molecules*, 2009, **14**, 423–438.
14 Y. Li and N. Gu, *J. Phys. Chem. B*, 2010, **114**, 2749–2754.
15 C. L. Ting and Z. G. Wang, *Biophys. J.*, 2011, **100**, 1288–1297.
16 J. Q. Lin, H. W. Zhang, Z. Chen and Y. G. Zheng, *ACS Nano*, 2010, **4**, 5421–5429.
17 J.-Q. Lin, Y.-G. Zheng, H.-W. Zhang and Z. Chen, *Langmuir*, 2011, **27**, 8323–8332.
18 J. P. Prates Ramalho, P. Gkeka and L. Sarkisov, *Langmuir*, 2011, **27**, 3723–3730.
19 Y. Li, X. Chen and N. Gu, *J. Phys. Chem. B*, 2008, **112**, 16647–16653.
20 S. L. Fiedler and A. Violi, *Biophys. J.*, 2010, **99**, 144–152.
21 R. Qiao, A. P. Roberts, A. S. Mount, S. J. Klaine and P. C. Ke, *Nano Lett.*, 2007, **7**, 614–619.
22 A. Alexeev, W. E. Uspal and A. C. Balazs, *ACS Nano*, 2008, **2**, 1117–1122.
23 K. Yang and Y. Q. Ma, *Nat. Nanotechnol.*, 2010, **5**, 579–583.
24 S. O. Nielsen, B. Ensing, V. Ortiz, P. B. Moore and M. L. Klein, *Biophys. J.*, 2005, **88**, 3822–3828.
25 M. Dutt, O. Kuksenok, S. R. Little and A. C. Balazs, *Nanoscale*, 2011, **3**, 240–250.
26 B. J. Reynwar, G. Illya, V. A. Harmandaris, M. M. Muller, K. Kremer and M. Deserno, *Nature*, 2007, **447**, 461–464.
27 H. D. Herce and A. E. Garcia, *Proc. Natl. Acad. Sci. U. S. A.*, 2007, **104**, 20805–20810.
28 T. Yue and X. Zhang, *Soft Matter*, 2011, **7**, 9104–9112.
29 O. S. Lee and G. C. Schatz, *J. Phys. Chem. C*, 2009, **113**, 2316–2321.
30 A. J. Makarucha, N. Todorova and I. Yarovsky, *Eur. Biophys. J.*, 2011, **40**, 103–115.
31 J. Gumbart, C. Chipot and K. Schulten, *Proc. Natl. Acad. Sci. U. S. A.*, 2011, **108**, 3596–3601.
32 C. E. Ashley, E. C. Carnes, G. K. Phillips, D. Padilla, P. N. Durfee, P. A. Brown, T. N. Hanna, J. W. Liu, B. Phillips, M. B. Carter, N. J. Carroll, X. M. Jiang, D. R. Dunphy, C. L. Willman, D. N. Petsev, D. G. Evans, A. N. Parikh, B. Chackerian, W. Wharton, D. S. Peabody and C. J. Brinker, *Nat. Mater.*, 2011, **10**, 389–397.
33 B. Zhao and L. Zhu, *Macromolecules*, 2009, **42**, 9369–9383.
34 F. Schreiber, *Prog. Surf. Sci.*, 2000, **65**, 151–256.
35 I. R. Cooke and M. Deserno, *J. Chem. Phys.*, 2005, **123**, 320–323.
36 I. R. Cooke, K. Kremer and M. Deserno, *Phys. Rev. E: Stat., Nonlinear, Soft Matter Phys.*, 2005, **72**, 011506.
37 G. Illya and M. Deserno, *Biophys. J.*, 2008, **95**, 4163–4173.

38 S. V. Bennun, M. I. Hoopes, C. Y. Xing and R. Faller, *Chem. Phys. Lipids*, 2009, **159**, 59–66.

39 C. Tanford, *Proc. Natl. Acad. Sci. U. S. A.*, 1979, **76**, 4175–4176.

40 M. P. Allen and D. J. Tildesley, *Computer simulation of liquids*, Clarendon Press; Oxford University Press, Oxford [Oxfordshire] New York, 1987.

41 D. A. McQuarrie, *Statistical mechanics*, University Science Books, Sausalito, Calif., 2000.

42 J. Zimmerberg and M. M. Kozlov, *Nat. Rev. Mol. Cell Biol.*, 2006, **7**, 9–19.

43 M. Deserno and T. Bickel, *Europhys. Lett.*, 2003, **62**, 767–773.

44 C. Nielsen, M. Goulian and O. S. Anderson, *Biophys. J.*, 1998, **74**, A309–A309.

45 C. Nielsen and O. S. Andersen, *Biophys. J.*, 2000, **79**, 2583–2604.

46 S. May, *Curr. Opin. Colloid Interface Sci.*, 2000, **5**, 244–249.

47 J. M. D. Lane and G. S. Grest, *Phys. Rev. Lett.*, 2010, **104**, 235501.

48 S. L. Zhang, J. Li, G. Lykotrafitis, G. Bao and S. Suresh, *Adv. Mater.*, 2009, **21**, 419.

49 S. V. Atre, B. Liedberg and D. L. Allara, *Langmuir*, 1995, **11**, 3882–3893.

50 C. Singh, P. K. Ghorai, M. A. Horsch, A. M. Jackson, R. G. Larson, F. Stellacci and S. C. Glotzer, *Phys. Rev. Lett.*, 2007, **99**, 226106.

51 J. P. Folkers, P. E. Laibinis, G. M. Whitesides and J. Deutch, *J. Phys. Chem.*, 1994, **98**, 563–571.

52 S. J. Stranick, A. N. Parikh, Y. T. Tao, D. L. Allara and P. S. Weiss, *J. Phys. Chem.*, 1994, **98**, 7636–7646.

53 A. V. Shevade, J. Zhou, M. T. Zin and S. Y. Jiang, *Langmuir*, 2001, **17**, 7566–7572.

54 K. Tamada, M. Hara, H. Sasabe and W. Knoll, *Langmuir*, 1997, **13**, 1558–1566.

55 C. Munuera and C. Ocal, *J. Chem. Phys.*, 2006, **124**, 206102.

56 P. K. Ghorai and S. C. Glotzer, *J. Phys. Chem. C*, 2010, **114**, 19182–19187.

57 J. P. K. Ghorai and S. C. Glotzer, *J. Phys. Chem. C*, 2007, **111**, 15857–15862.

58 R. J. K. U. Ranatunga, R. J. B. Kalescky, C. C. Chiu and S. O. Nielsen, *J. Phys. Chem. C*, 2010, **114**, 12151–12157.

59 S. Berger, A. Synytska, L. Ionov, K. J. Eichhorn and M. Stamm, *Macromolecules*, 2008, **41**, 9669–9676.

60 Y. Guo and M. G. Moffitt, *Macromolecules*, 2007, **40**, 5868–5878.

61 D. Li, X. Sheng and B. Zhao, *J. Am. Chem. Soc.*, 2005, **127**, 6248–6256.

62 E. W. Edwards, M. Chanana, D. Wang and H. Mohwald, *Angew. Chem., Int. Ed.*, 2008, **47**, 320–323.

63 K. S. Iyer, B. Zdyrko, S. Malynych, G. Chumanov and I. Luzinov, *Soft Matter*, 2011, **7**, 2538–2542.

64 B. J. Kim, G. H. Fredrickson, C. J. Hawker and E. J. Kramer, *Langmuir*, 2007, **23**, 7804–7809.

65 D. J. Li and B. Zhao, *Langmuir*, 2007, **23**, 2208–2217.

66 A. Walther and A. H. E. Muller, *Soft Matter*, 2008, **4**, 663–668.

67 A. Walther, C. Barner-Kowollik and A. H. E. Muller, *Langmuir*, 2010, **26**, 12237–12246.

68 C. LoPresti, M. Massignani, C. Fernyhough, A. Blanazs, A. J. Ryan, J. Madsen, N. J. Warren, S. P. Armes, A. L. Lewis, S. Chirasatitsin, A. J. Engler and G. Battaglia, *ACS Nano*, 2011, **5**, 1775–1784.

69 K. L. Genson, J. Holzmueller, C. Y. Jiang, J. Xu, J. D. Gibson, E. R. Zubarev and V. V. Tsukruk, *Langmuir*, 2006, **22**, 7011–7015.

70 E. R. Zubarev, J. Xu, A. Sayyad and J. D. Gibson, *J. Am. Chem. Soc.*, 2006, **128**, 4958–4959.